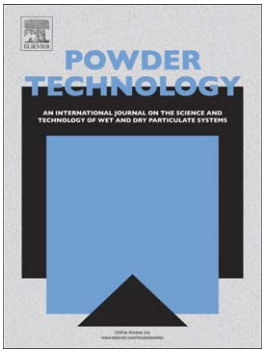

Particle statistics in a two-way coupled turbulent boundary layer flow over a flat plate

Dong Li, Kun Luo, Jianren Fan

PII: S0032-5910(16)30647-7
DOI: doi:10.1016/j.powtec.2016.09.063
Reference: PTEC 11973

To appear in: *Powder Technology*

Received date: 26 July 2016
Revised date: 19 September 2016
Accepted date: 26 September 2016

Please cite this article as: Dong Li, Kun Luo, Jianren Fan, Particle statistics in a two-way coupled turbulent boundary layer flow over a flat plate, *Powder Technology* (2016), doi:10.1016/j.powtec.2016.09.063

Particle statistics in a two-way coupled turbulent boundary layer flow over a flat plate

By

Dong Li, Kun Luo*, Jianren Fan

State Key Laboratory of Clean Energy Utilization, Zhejiang University, Hangzhou 310027, PR China

Submitted to

Powder Technology

* Correspondence to: Kun Luo, State Key Laboratory of Clean Energy Utilization, Zhejiang University, 38 Zheda Road, Hangzhou, PR China. Fax: +86-0571-87951764; E-mail: zjulk@zju.edu.cn

ABSTRACT

In the present study, we investigate heavy solid particle statistics in a spatially developing turbulent boundary layer over a flat plate using the two-way coupled Eulerian-Lagrangian point-particle approach. The particles are much smaller than the Kolmogorov length scale in the dilute gas-solid flow. The simulation results show that the particle streamwise fluctuating velocity exceeds the fluid streamwise fluctuating velocity across the entire boundary layer. In the wall-normal and spanwise directions, however, the velocity fluctuations of the particles generally tend to be lower than those of the fluid. Moreover, the particle wall-normal and spanwise fluctuating velocities decrease monotonically with particle Stokes number and mass loading. In addition, it is found that the spatial evolution of the particle wall concentration along the streamwise direction is similar to that of the mean skin-friction coefficient. These new findings are of great importance in the industrial and environmental applications.

Keywords: particle statistics, two-way coupled simulation; turbulent boundary layer; particle wall concentration

Introduction

Particle-laden turbulent flows are frequently encountered in a wide range of industrial and environmental applications, such as coal combustion, pollutant dispersion and pneumatic conveyance, etc. In spite of extensive numerical and experimental investigation, the particle dynamics in wall-bounded flows have still not been completely understood and many issues remain wide open.

In wall-bounded flows, one of the most interesting phenomena is particle preferential accumulation close to the wall, which is called turbophoresis, initially proposed by Caporaloni et al. [1] and further investigated by Reeks [2]. Kaftori et al. [3] studied particle behavior in the wall region of a turbulent boundary layer by flow visualization techniques and laser Doppler anemometry. They found that the motion of solid particles was controlled by the action of coherent wall structures. Subsequently, many researchers confirmed that the sweep and ejection events, generated by near-wall quasi-streamwise vortical structures, were responsible for particle accumulation in the viscous sublayer [4-7]. It should be pointed out that even in the near-wall region, particle distribution is not uniform. Instead, the particles immersed within the viscous sublayer preferentially accumulate along the low-speed streaks [8-11]. Recently, the exhaustive reviews of the experimental and numerical studies of turbophoresis phenomenon were given by Soldati and Marchioli [12] and Balachandar and Eaton [13].

In addition to the qualitative characteristics, i.e. turbophoresis, the quantitative statistics for the particle phase have also been investigated during the past few decades [14-17]. However, there is a lack of unanimity among the findings from these research studies.

Among these experimental and numerical investigation, most focus on parallel flows such as channel or pipe flows, in which the motion of particles is assumed to be periodic along the flow direction. However, very little research has been reported on particle dynamics in a spatially developing boundary layer flow. Tanière et al. [18] investigated experimentally the behavior of solid particles in a horizontal boundary layer over a flat plate. Recently, Sardina et al. [19] exploited a one-way coupled simulation for particle dynamics in a spatially developing turbulent boundary layer up to $Re_\theta = 2500$. They observed a self-similar behavior of the wall-normal particle concentration and streamwise velocity profiles in the outer region of the boundary layer. It should be mentioned that this is the first attempt to investigate particle statistics in a flat-plate boundary layer by means of a two-way coupled direct numerical simulation (DNS). Several simulations are carried out to examine the effects of particle Stokes number and mass loading on particle statistics in a spatially evolving boundary layer.

The structure of the paper is as follows. First, we describe the mathematical model and numerical methodology in section 2. Then in section 3, the simulation results of the mean and fluctuating quantities for the particle phase are presented and

analyzed. The accumulation characteristics of particles are investigated in detail in section 4. Finally, the main findings are summarized and the conclusions are drawn in section 5.

1. Mathematical model and methodology

2.1. Equations of fluid phase

In this study, the air (regarded as incompressible and Newtonian) with density $\rho_f = 1.205\ \mathrm{kg\,m^{-3}}$ and kinematic viscosity $\nu = 1.5\times10^{-5}\ \mathrm{m^2\,s^{-1}}$ is considered. Since the diameter of the largest particle is much smaller than the smallest grid scale, the momentum coupling effect on the fluid by dispersed particles can be approximated by a point force. Therefore, the dimensionless continuity and momentum equations for the fluid can be expressed as

$$\nabla\cdot\mathbf{u} = 0, \tag{1}$$

$$\frac{\partial\mathbf{u}}{\partial t} + \mathbf{u}\cdot\nabla\mathbf{u} = -\nabla p + \frac{1}{Re_{\theta_0}}\nabla^2\mathbf{u} + \mathbf{f}, \tag{2}$$

where $\mathbf{u} = (u, v, w)$ and p are the instantaneous fluid velocity vector and fluctuating kinematic pressure, respectively. $Re_{\theta_0} = U_\infty\theta_0/\nu$ is the inlet momentum thickness Reynolds number based on the free stream velocity U_∞, the inlet momentum thickness θ_0 and the kinematic viscosity ν. For the two-way coupled simulations, $\mathbf{f}$ represents the particle-to-fluid feedback force in the control volume.

The Navier-Stokes and continuity equations are solved using a fractional step algorithm on staggered grids [20]. The diffusion terms in the wall-normal direction

are integrated in time implicitly using a second-order Crank-Nicolson scheme, while the convection and wall-parallel diffusion terms are treated explicitly using a low-storage, third-order Runge-Kutta scheme. The spatial derivatives in the convective terms of the momentum equation are discretized with a fourth-order accurate finite difference scheme and the viscous terms are discretized with a high-order Lagrange interpolating polynomial [21, 22]. The BiConjugate Gradient Stablized (BICGSTAB) solver with multigrid preconditioner is employed to solve the pressure Poisson equation.

Fig. 1 shows a schematic of the particle-laden turbulent boundary layer flow over a flat plate. The origin of the Cartesian coordinate system is located on the wall at the leading edge of the plate. The dimensions of the computational domain are $L_x \times L_y \times L_z = 6375\theta_0 \times 1500\theta_0 \times 375\theta_0$ with $4096 \times 512 \times 128$ grid points in the streamwise (x), wall-normal (y) and spanwise (z) directions, respectively. The laminar inlet is located at $Re_{\theta_0} = 80$. All the grids are uniform in the streamwise and spanwise directions. The streamwise resolution, $\Delta x^+ = 5.91$, is close to the resolution used in references [23-25], but much higher than that in references [26, 27]. The spanwise resolution, $\Delta z^+ = 11.13$, is comparable to that used in references [23, 28]. Note that the variables written in wall units (identified by superscript $+$) are non-dimensionalized based on the wall-friction velocity $u_\tau = 0.0475$ at the turbulent station $Re_\theta = 900$. The wall-normal grid is stretched using a hyperbolic-tangent function to resolve the near-wall boundary layer flow and the first grid point away from

the wall is at $\Delta y^+_{min} = 0.69$. The dimensionless computational time step used is $\Delta t^+ = 0.09$. The simulations were carried out using 1024 processors on 64 IBM 16-way nodes. All the statistical results presented in this paper have been averaged over time and over the homogeneous spanwise direction.

At the laminar inlet, the isotropic turbulence box is introduced into the computational domain every $3000\Delta t$ in order to trigger a laminar boundary layer to transition. The size of the isotropic turbulence box is $375\theta_0$ in each direction. Note that the isotropic turbulent velocity field, with turbulence intensity of 8.3%, is obtained from a precursor DNS computation of decaying homogenous isotropic turbulence. At the inlet, the velocity fluctuations of the isotropic turbulence are superimposed on the free stream velocity ($15\theta_0$ away from the wall) so that the Blasius boundary layer could not be distorted by the imposed perturbations. A convective boundary condition is applied to each velocity component at the outflow plane $x = 6556.5\theta_0$. The no-slip conditions, $u = 0, v = 0, w = 0$, are enforced at the wall. Periodic boundary conditions are imposed in the spanwise direction. At the top of the computational domain, the boundary conditions are $u = U_\infty$, $v = V_{Blasius}$ and $w = 0$. The velocity corrections are made at the exit plane to ensure global mass conservation.

2.2. Equations of particle phase and Lagrangian particle tracking

Regarding the dispersed phase, we assume that all particles are pointwise, rigid spheres with identical diameter d_p and density ρ_p. The particle concentration is dilute and the inter-particle collision effect can be ignored. The solid particles are

much smaller than the Kolmogorov length scale and the density ratio of the particle to fluid is taken to be 1500. A corresponding physical case is, for example, the pneumatic transport of $50 \sim 100 \mu m$ coal particles along the plate. To focus on particle-fluid interactions, gravity is neglected. Based on these assumptions, the drag force is the significant force on a solid particle [29, 30]. Other forces acting on the particles, such as buoyancy force, pressure gradient force, Basset force and virtual mass force are assumed to be negligible in our simulations (orders of magnitude smaller than the drag force). In the present boundary layer flows, the slip-rotation lift force and the slip-shear lift force are also taken into account due to the particle-wall collision effect and the strong shear flows in the near-wall regions. Therefore, the Lagrangian equations to govern the particle motion can be expressed as follows

$$\frac{\mathrm{d}\mathbf{x}_p}{\mathrm{d}t} = \mathbf{u}_p, \tag{3}$$

$$m_p \frac{\mathrm{d}\mathbf{u}_p}{\mathrm{d}t} = \mathbf{F}_D + \mathbf{F}_{LS} + \mathbf{F}_{LR}, \tag{4}$$

$$I_p \frac{\mathrm{d}\boldsymbol{\omega}_p}{\mathrm{d}t} = \mathbf{T}, \tag{5}$$

where $\mathbf{x}_p$, $\mathbf{u}_p$ and $\boldsymbol{\omega}_p$ are coordinate, linear and angular velocity vectors of the particles, respectively. m_p is the mass of the particle and I_p is the moment of inertia. $\mathbf{F}_D$, $\mathbf{F}_{LS}$, $\mathbf{F}_{LR}$ and $\mathbf{T}$ respectively denote the drag force, the slip-shear lift force, the slip-rotation lift force and the torque acting on the particles. The drag force is given as

$$\mathbf{F}_D = \frac{\rho_f}{2}\frac{\pi}{4} d_p^2 C_D \left|\mathbf{u}_f - \mathbf{u}_p\right| (\mathbf{u}_f - \mathbf{u}_p), \tag{6}$$

where $\mathbf{u}_f$ is the fluid velocity vector at the position of the particle. The drag coefficient C_D is calculated from the correlation [31]

$$C_D = \frac{24}{Re_p}\left(1 + 0.15 Re_p^{0.687}\right), \tag{7}$$

where $Re_p = d_p \left|\mathbf{u}_f - \mathbf{u}_p\right| / \nu$ is the particle Reynolds number. The slip-shear lift force is obtained according to Mei [32] in the form

$$\mathbf{F}_{LS} = \frac{\rho_f}{2}\frac{\pi}{4} d_p^3 C_{LS} \left\{\left(\mathbf{u}_f - \mathbf{u}_p\right) \times \boldsymbol{\omega}_f\right\}, \tag{8}$$

where $\boldsymbol{\omega}_f = 1/2 \nabla \times \mathbf{u}_f$ is the angular velocity vector of the fluid and the lift coefficient C_{LS} is computed as follows

$$C_{LS} = \frac{4.1126}{Re_s^{0.5}} f(Re_p, Re_s), \tag{9}$$

where $Re_s = d_p^2 \left|\boldsymbol{\omega}_f\right| / \nu$ is the Reynolds number of the shear flow. $f(Re_p, Re_s)$ is explained as a ratio of the extended lift force to the Saffman lift force

$$f(Re_p, Re_s) = \begin{cases} (1 - 0.3314\beta^{1/2}) \exp\left(-\dfrac{Re_p}{10}\right) + 0.3314\beta^{1/2} & Re_p \le 40, \\ 0.0524(\beta Re_p)^{1/2} & Re_p > 40, \end{cases} \tag{10}$$

where the parameter β is expressed as

$$\beta = \frac{d_p \left|\boldsymbol{\omega}_f\right|}{2\left|\mathbf{u}_f - \mathbf{u}_p\right|} = \frac{1}{2}\frac{Re_s}{Re_p}. \tag{11}$$

The slip-rotation lift force was proposed by Crowe et al. [33] as

$$\mathbf{F}_{LR}=\frac{\rho_f}{2}\frac{\pi}{4}d_p^2C_{LR}\left|\mathbf{u}_f-\mathbf{u}_p\right|\frac{\boldsymbol{\Omega}\times\left(\mathbf{u}_f-\mathbf{u}_p\right)}{\left|\boldsymbol{\Omega}\right|}, \tag{12}$$

where $\boldsymbol{\Omega}=\boldsymbol{\omega}_f-\boldsymbol{\omega}_p$ represents the relative rotation between fluid and particle. C_{LR} is the slip-rotation lift coefficient. According to Rubinow and Keller [34] and Oesterle and Dinh [35], it is formulated as

$$C_{LR}=\begin{cases}\dfrac{Re_R}{Re_p} & Re_p\le 1,\\ 0.45+\left(\dfrac{Re_R}{Re_p}-0.45\right)\exp\left(-0.05684Re_R^{0.4}Re_p^{0.3}\right) & 1<Re_p<140,\end{cases} \tag{13}$$

where $Re_R=d_p^2\left|\boldsymbol{\Omega}\right|/\nu$ is the Reynolds number of particle rotation. The torque acting on a rotating particle is calculated from

$$\mathbf{T}=\frac{\rho_f}{2}\left(\frac{d_p}{2}\right)^5C_R\left|\boldsymbol{\Omega}\right|\boldsymbol{\Omega}, \tag{14}$$

where the rotational coefficient C_R is written according to previous research results [34, 36, 37] as

$$C_R=\begin{cases}\dfrac{64\pi}{Re_R} & Re_R\le 32,\\ \dfrac{12.9}{Re_R^{0.5}}+\dfrac{128.4}{Re_R} & 32<Re_R<1000.\end{cases} \tag{15}$$

In the present study, two-way coupling is assumed to model the particle-fluid interactions since the particle volume fraction Φ_v is large enough to modulate the turbulence, i.e. $6.67\times10^{-5}\le\Phi_v\le6.67\times10^{-4}$. The feedback force exerted by the particles on the Eulerian grid point m in Eq. (2) read as

$$\mathbf{f}_m = -\sum_{n=1}^{N_p} \frac{\rho_p V_p}{\rho_f V_m} \mathbf{f}_p^n S\left(\mathbf{x}^n, \mathbf{x}^m\right), \tag{16}$$

where N_p is the instantaneous number of particles within the control volume. V_p and V_m are respectively the volume of particle n and the control volume of fluid grid m. $\mathbf{f}_p^n$ denotes the total force acting on particle n. The weight function $S\left(\mathbf{x}^n, \mathbf{x}^m\right)$ locally distributes the total force $\mathbf{f}_p^n$ between particle n and fluid grid m via a fourth-order Lagrangian interpolation scheme.

The initial velocity field throughout the domain is identical to a fully developed instantaneous velocity field obtained by DNS of a single-phase spatially developing turbulent boundary layer over a flat plate. At the beginning of the Lagrangian tracking, a great number of particles $O(10^8 \sim 10^9)$ are distributed randomly over the computational domain both inside and outside the boundary layer zone ($0 < y \le 120\theta_0$), and their initial velocities are set equal to those of the fluid at the particle initial position. Since particles are not restricted to lie on the Eulerian grid points, the fourth-order Lagrange interpolating polynomials are employed to evaluate the fluid velocity at the particle position. In order to maintain a constant mass loading of particles, when a particle exits the computational domain from the outlet, another particle is randomly released into the domain from the inlet. The height of the computational domain is large enough that no particles move out of the domain from the top boundary. Particles exiting the computational domain along the spanwise direction are reintroduced via periodicity. The perfectly elastic collisions at the flat plate are assumed when one

particle center is less than a distance $d_p/2$ from the wall. For more details on the particle-wall collisions, the reader is referred to Yamamoto et al. [38].

In this context, we adopt the Eulerian-Lagrangian point-particle approach to simulate the particle-laden turbulent flows. The trajectories of the particles are tracked individually through the integration of Eq. (3) by a second-order Crank-Nicolson scheme. An explicit third-order Runge-Kutta scheme is used for time integration of the particle linear and angular velocities. In the particle-laden flows, the main parameter that controls the dynamics of particles is the so-called Stokes number St, which is the ratio between the particle relaxation time τ_p and a characteristic time scale of the fluid τ_f:

$$St = \frac{\tau_p}{\tau_f} = \frac{\rho_p d_p^2 / 18\mu}{\theta_0 / U_\infty}, \tag{17}$$

where μ is the dynamic viscosity of the fluid. In order to investigate particle statistics in a spatially developing turbulent boundary layer, three particle populations characterized by different Stokes numbers and different mass loadings are considered in this work. Table 1 reports the parameters of the tracked particles in the three different simulations, with the particle Stokes number St, the mass loading Φ_m, the particle diameter in wall unit d_p^+, the total number of particles $N_{p,total}$, the ratio of the smallest grid scale Δy_{min} to the particle diameter d_p, and the ratio between the minimum Kolmogorov length scale η_{min} and the particle diameter d_p. The smallest grid cell is significantly larger than the size of particles whereas smaller than the

Kolmogorov length scale, i.e. $d_p < \Delta y_{min} < \eta_{min}$, and thus it fulfills the requirements imposed by point-particle DNS approach [39].

2. Particle velocity statistics

In this section, we present the statistics results of the mean and fluctuating velocities for the dispersed phase in the two-way coupled particle-laden flows over a flat plate. The comparisons of the results for different simulations are carried out to investigate the effects of particle Stokes number and mass loading on the velocity statistics of the particles. Before presenting the DNS results, we first validate our numerical results of single-phase and particle-laden flows. Fig. 2 shows the comparisons of the mean streamwise velocity and the turbulence intensities between our single-phase results and previous experimental and numerical results in the literature. Clearly, the present single-phase numerical results agree very well with those experimental results of Adrian et al. [40] and Ching et al. [41], and the numerical data of Wu and Moin [23]. In order to validate our two-way coupled DNS results, Fig. 3 compares the numerical results of Case A at $Re_\theta = 900$ with the boundary layer experimental data of Rogers and Eaton [42] at $Re_\theta = 1090$. Considering that the particle and fluid parameters are different between the two datasets, the agreement is reasonable.

Fig. 4 displays the mean streamwise particle velocity profiles versus the inner wall coordinate y^+ and the outer coordinate y/δ at the same streamwise location $x = 4867\theta_0$. It can be noticed that the mean streamwise particle velocity $\overline{u}_p$ increases monotonically with the particle mass loading Φ_m and Stokes number St, except

for the region close to the wall where the particles in case B with smaller inertia $St = 10$ have a higher velocity than those in case C with larger inertia $St = 50$. The relative mean streamwise velocity between particles and fluid obtained at $x = 4867\theta_0$ is presented in Fig. 5, using a semi-logarithmic scale. The mean fluid velocity $\bar{u}_f$ is larger than the mean particle velocity $\bar{u}_p$ in the buffer layer, while the reverse is true in the region far away from the wall. As the particle mass loading increases, the velocity difference between the solid phase and the gas phase increases. It is particularly noteworthy that in the logarithmic layer, the profile in case C with larger inertial particles $St = 50$ exhibits a remarkable peak, which is approximately five times larger than that in other two cases with smaller inertial particles. This is probably due to the inertial effects. As it is known, the inertial particles tend to retain their velocities initially obtained from the fluid field and the effect is intensified with increasing particle Stokes number. Therefore, the particle population characterized by larger Stokes number has a greater velocity than the fluid.

Fig. 6 reports the profiles of particle fluctuating velocities and Reynolds stress versus the inner wall coordinate y^+ at $x = 4867\theta_0$. The velocity fluctuations and Reynolds stress of the fluid phase are also included in this figure for a quantitative comparison. In Fig. 6(a) only the fluid velocity fluctuation of case B is presented for better visibility, other cases exhibit similar characteristics to case B. It is seen apparently that the particle streamwise fluctuating velocity $u'^+_{p\,rms}$ is larger than the fluid streamwise fluctuating velocity $u'^+_{f\,rms}$ across the entire boundary layer, which is con-

sistent with the experimental results of Tanière et al. [18] in a horizontal boundary layer over a flat plate.

In contrary to the streamwise component, the wall-normal fluctuating velocity of the particles $v'^{+}_{p\,rms}$ is lower than that of the fluid $v'^{+}_{f\,rms}$ for the cases with smaller inertial particles. This is probably because the solid particles could not fully respond to all the turbulent eddies of fluid due to their inertia, and thus the fluid phase tends to fluctuate much more than the solid phase in the wall-normal direction. In case C with larger inertial particles $St = 50$, the particle wall-normal fluctuating velocity slightly increases in the wall region with $y^{+} < 8$, while decreases in the $y^{+} > 8$ region compared with the fluid wall-normal fluctuating velocity. In addition, it is evident that the wall-normal velocity fluctuation of the particles decreases with increasing particle Stokes number St and mass loading Φ_m, and so is the wall-normal fluctuating velocity of the fluid.

Concerning the spanwise component of the velocity fluctuation, it is observed in Fig. 6(c) that there has nearly no significant difference between the fluid and particle fluctuating velocities in the cases with smaller Stokes number. When increasing the particle Stokes number, however, the fluid turbulent fluctuation exceeds the particle velocity fluctuation throughout the whole boundary layer along the spanwise direction (case C). This trend can also be explained by the particle inertial effects as discussed above. As the particle Stokes number and mass loading increase, both the particle and fluid spanwise fluctuating velocities decrease across the entire boundary layer.

The Reynolds stress profiles for both the particle phase and fluid phase are shown in Fig. 6(d). As expected, the profiles of particle Reynolds stress are similar to those of fluid. However, the particle Reynolds stress is larger than the fluid Reynolds stress in all three different cases. Moreover, both the particle and fluid Reynolds stresses decrease with increasing particle mass loading and Stokes number.

A physical explanation of the behavior of particles is provided in Fig. 7, where the instantaneous distributions of the particle populations with $St = 50$, are superposed on the local streamwise vorticity field ω_x. The vectors represent the particle velocities in the *y*-*z* plane at $x = 4867\theta_0$. The particles are indicated by solid circles, larger than the real scales for better visualization: white circles represent the particles moving away from the wall, while red circles represent the particles migrating towards the wall. The vortical structures are identified by the instantaneous contours of the streamwise vorticity: dark blue color indicates counterclockwise-rotating quasi-streamwise vortices, whereas red color indicates clockwise-rotating quasi-streamwise vortices. In the turbulent boundary layer, as depicted in Fig. 7, a great number of inertial particles are moved towards the wall by the large-scale rotating quasi-streamwise vortices with a strong sweep event. And meanwhile, some of them are transferred away from the wall by an ejection event generated by the same quasi-streamwise vortices. The unbalance between the number of incoming and outgoing particles gives rise to a high particle concentration in the near-wall region. On the other hand, the inertial particles tend to maintain their velocities. On average, the up-

wards moving particles have smaller streamwise velocities whereas the downwards moving particles possess larger velocities. Under the action of near-wall quasi-streamwise vortices, the particles from the outer layer with higher velocities migrate towards the wall and apparently enhance the local particle streamwise velocity fluctuations. Of course, since the particles entering the outer layer from the wall region tend to retain their lower velocities, the streamwise velocity fluctuation of the particles is augmented as well in the outer region of the boundary layer. We can therefore conclude that it is the combined effect of particle inertia and near-wall vortical structures that is mainly responsible for the increase in the streamwise fluctuating velocity of the particles.

One may ask why the upward and downward movements of inertial particles increase the streamwise fluctuating velocity of the solid phase, while the velocity fluctuations of the particles tend to be less than those of the fluid in the spanwise and wall-normal directions. As noted before, the sweep and ejection events enhance the mixing and exchange of low-speed and high-speed particles between the near-wall region and the region outside. It should be pointed out that the velocity difference between the wall layer and the outer layer is quite small in the spanwise and wall-normal directions. Therefore, the migration of particles has almost no pronounced effect on the particle velocity fluctuations in the directions perpendicular to the mean flow.

As stated above, the particle fluctuation level is higher than the fluid in the streamwise direction. In the directions perpendicular to the mean flow, however, the velocity fluctuations of the particles generally tend to be less than those of the fluid, especially in the region away from the wall. To give a further comparison of the velocity fluctuation between particles and fluid, Fig. 8 displays the wall-normal distribution of the ratio between the particle turbulent kinetic energy K_p and the fluid turbulent kinetic energy K_f in the turbulent region at $x = 4867\theta_0$. Note that K_f is defined as $K_f = 1/2\left(u_f'^2 + v_f'^2 + w_f'^2\right)$, and K_p can be expressed in a similar manner. The turbulent kinetic energy of the particles is greater than that of the fluid in the near-wall region, while $K_p < K_f$ is true in the wake region of the boundary layer. On the one hand, the near-wall quasi-streamwise vortices transfer the particles with higher velocities towards the wall. On the other hand, the fluid phase fluctuations tend to vanish in the close vicinity of the wall due to the no-slip condition at the wall. However, the solid phase does not need to satisfy the condition imposed by the wall. Considering that the highest particle concentration is found at the wall, it is expected in Fig. 8 that the maximum ratio of K_p to K_f is obtained at the wall. In the buffer and logarithmic layers, the particle turbulent kinetic energy K_p is slightly larger than the energy of the fluid phase K_f, since the streamwise velocity fluctuation of the particles is higher than that of the fluid, as mentioned above. The fact that K_p is less than K_f in the wake region may be explained by the decrease of the particle velocity fluctuations in the wall-normal and spanwise directions compared with the fluid

one. It is interesting to note that the fluid turbulent kinetic energy is again less than the particles in the region further away from the turbulent boundary layer ($y^+ > 500$). As a matter of fact, the fluid velocity in the $y^+ > 500$ region is approximately identical to the free stream velocity, and thus the fluid phase fluctuations almost disappear completely. Due to inertia, the solid phase still remains large fluctuating velocity in the free stream velocity field. As a consequence, another peak of the ratio between K_p and K_f is observed in the region with $y^+ > 500$.

3. Particle concentration

In wall-bounded flows, the inertial particles tend to migrate towards the wall and this behavior has been investigated numerically and experimentally during the past few decades [3-5]. Different from channel and pipe flows in which the particle motion is regarded as periodic along the flow direction, the boundary layer flow develops spatially and the motion of particles is thus assumed to be non-periodic in the streamwise direction.

The streamwise development of the particle concentration at the wall C_w along the flat plate is depicted in Fig. 9. The mean skin-friction coefficient C_f is also plotted on the same axes for a comparison. In this paper, the wall concentration of the particles C_w is defined as the number of particles within the control volume below a distance of $y^+ = 0.69$ from the wall, i.e. the closest grid cell to the wall. The mean skin-friction coefficient is given as $C_f = 2\tau_w / \rho U_\infty^2$, where $\tau_w = \mu \partial \overline{u} / \partial y|_{y=0}$ is the mean wall shear stress. It is interesting to note that the profiles of the wall concentra-

tion C_w are similar to the distributions of C_f. It is widely accepted that the laminar, transitional and turbulent regions can be determined by the skin-friction coefficient in boundary layer flow, i.e. the start and end of the transition are respectively identified by the local minimum and maximum of C_f [43, 44]. As indicated in Fig. 9, the wall concentration decreases rapidly in the laminar region characterized by a large streamwise gradient of C_w, until the location of the onset of transition where a local minimum of wall concentration is observed.

During the transitional stage, however, the particle concentration C_w increases gradually along the flow direction. In the vicinity where transition is complete, a distinct peak is attained in the streamwise distribution of the wall concentration. In particular, the peak position in case B corresponds completely to the location at which the completion of transition occurs. It is worthy to note that the location of the peak value of wall concentration in case B is nearly the same as that in case C, irrespective of particle mass loading. This means that the peak location of wall concentration may just only depend on particle inertia, and the concentration peak moves downstream when increasing the particle Stokes number, since the particle populations with larger inertia obviously delay the completion of transition, as shown in Fig. 9(b). In addition, it is also observed that the intensity of the concentration peak grows as the particle inertia and mass loading increase. Downstream of the concentration peak, the particle wall concentration decreases slowly with increasing Re_θ, especially in the fully developed turbulent region, as is the mean skin-friction coefficient.

One of the main findings in this study is that the evolution of the wall concentration along the flow direction follows a similar trend to the variation of the mean skin-friction drag. Considering that the gravity is not taken into account, the behavior of particle deposition at the wall should be associated with near-wall vortical structures. In order to explain the physical mechanisms responsible for the distributions of particle wall concentration, Fig. 10 shows instantaneous snapshots of the three-dimensional vortical structures inside the flat-plate boundary layer for case B. Note that the vortical structures, colored by the streamwise fluid velocity, are identified using the isosurfaces of the second invariant of the velocity gradient tensor, Q [45]. As shown in Fig. 10(a), the Λ-shaped vortex structure, induced by the isotropic turbulent perturbations, obviously exists near the wall in the laminar regime of $600\theta_0 \le x \le 800\theta_0$. Then the Λ-shaped vortices evolve and ultimately develop into the hairpin-shaped vortices as it is convected downstream. In Fig. 10(b), several individual hairpin vortices with different size align behind each other in the streamwise direction and form a turbulent spot in the transitional region of $1400\theta_0 \le x \le 2200\theta_0$. These turbulent spots grow as they move downstream, merge into one another and span the whole boundary layer in the early turbulent region (Fig. 10c). In the vicinity of the skin-friction maximum, the hairpin vortices occur in streamwise-aligned packets, i.e. the hairpin packets. As seen in Fig. 10(d), the highly organized hairpin packets fill the boundary layer and become the dominant flow structure in the fully developed turbulent region.

As shown in Fig. 7, the near-wall quasi-streamwise vortices are responsible for particle accumulation in the near-wall region. On the other hand, it is known that the hairpin vortices consist of a pair of counter-rotating quasi-streamwise vortices, i.e. two legs, which are jointed through a head segment [46, 47]. Thus, the hairpin-shaped vortical structures are strongly associated with the distributions of the particle wall concentration. In the transitional region, the increase in the wall concentration along the streamwise direction is probably due to the fact that the number of hairpin vortices increases progressively as they move downstream. The turbulent boundary layer is densely populated by the forests of hairpins and thus the decrease rate of the particle wall concentration obviously reduces in the fully developed turbulent region. Considering that C_w decreases slowly along the flow direction, it can be inferred that the coherent vortical structures will gradually diminish or even disappear as the flow develops downstream. In other words, the coherency of vortical structures will be completely lost at very high Reynolds number and eventually the particles will behave as tracers without preferential accumulation.

4. Conclusions

In this context, three cases with different particle Stokes numbers and different mass loadings have been simulated and compared in order to investigate heavy solid particle statistics in a spatially developing flat-plate boundary layer. It is found that the solid phase tends to fluctuate much more than the fluid phase in the entire boundary layer along the streamwise direction. This trend can be explained in terms of the

combined effect of particle inertia and near-wall quasi-streamwise vortices. However, the velocity fluctuations of the particles generally tend to be less than those of the fluid in the spanwise and wall-normal directions, since the inertial particles could not fully respond to all the turbulent eddies in the fluid field. Furthermore, the particle wall-normal and spanwise fluctuating velocities decrease monotonically with particle Stokes number and mass loading.

A peculiar feature of particle-laden boundary layer flow is that the distributions of the particle wall concentration along the flat plate are similar to those of the mean skin-friction coefficient. The wall concentration attains a minimum value at the location where the onset of transition occurs and obtains a local maximum value in the vicinity where transition is complete. In the transitional region, the wall concentration gradually increases along the streamwise direction due to the effect of near-wall vortical structures. However, the particle wall concentration decreases slowly with the streamwise distance in the fully developed turbulent region. We can therefore infer that the coherency of vortical structures will be gradually reduced or even lost as the flow develops downstream, and eventually particles will behave as passive tracers without preferential accumulation. These new findings are of great significance to enhance the understanding of particle behavior in turbulent boundary layer flow.

Acknowledgements

This work is supported by the National Natural Science Foundation of China (No. 51136006). We are grateful to that.

Nomenclature

C_D drag coefficient

C_f skin-friction coefficient

C_{LR} slip-rotation lift coefficient

C_{LS} slip-shear lift coefficient

C_R rotational coefficient

C_w particle wall concentration

d_p particle diameter

$\mathbf{f}$ particle-to-fluid feedback force

$\mathbf{F}_D$ drag force

$\mathbf{F}_{LR}$ slip-rotation lift force

$\mathbf{F}_{LS}$ slip-shear lift force

I_p particle moment of inertia

K turbulent kinetic energy

L_x, L_y, L_z dimensions of the computational domain in the streamwise, wall-normal and spanwise directions

m_p particle mass

N_p the number of particles

p fluctuating kinematic pressure

Re_p particle Reynolds number

Re_R rotational Reynolds number

Re_s shear Reynolds number

Re_θ momentum thickness Reynolds number

Re_{θ_0} inlet momentum thickness Reynolds number

St particle Stokes number

$\mathbf{T}$ particle torque

$\mathbf{u}$ velocity vector

u, v, w instantaneous velocity components in the streamwise, wall-normal and spanwise directions

u_τ wall-friction velocity

U_∞ free stream velocity

V_p particle volume

x, y, z Cartesian coordinates in the streamwise, wall-normal and spanwise directions

Greek symbols

δ boundary layer thickness

δ^* displacement thickness

Δt computational time step

Δx streamwise grid spacing

Δy_{min} minimum wall-normal grid spacing

Δz spanwise grid spacing

η_{min} minimum Kolmogorov length scale

θ_0 inlet momentum thickness

μ dynamic viscosity

ν kinematic viscosity

ρ density

τ_f characteristic flow time scale

τ_p particle relaxation time

τ_w mean wall shear stress

Φ_m particle mass loading

Φ_v particle volume fraction

$\boldsymbol{\omega}$ angular velocity vector

$\boldsymbol{\Omega}$ relative rotational velocity

Subscripts and superscripts

f fluid

p particle

$+$ normalized by wall units

$'$ fluctuating part

$\overline{}$ average over time and over the spanwise direction

References

[1] M. Caporaloni, F. Tampieri, F. Trombetti, O. Vittori, Transfer of particles in nonisotropic air turbulence, J. Atmos. Sci. 32 (1975) 565-568.

[2] M. Reeks, The transport of discrete particles in inhomogeneous turbulence, J. Aerosol Sci. 14 (1983) 729-739.

[3] D. Kaftori, G. Hetsroni, S. Banerjee, Particle behavior in the turbulent boundary-layer .1. motion, deposition, and entrainment, Phys. Fluids 7 (1995) 1095-1106.

[4] J.B. McLaughlin, Aerosol particle deposition in numerically simulated channel flow, Phys. Fluids A 1 (1989) 1211.

[5] C. Marchioli, A. Soldati, Mechanisms for particle transfer and segregation in a turbulent boundary layer, J. Fluid Mech. 468 (2002) 283-315.

[6] H.F. Zhang, G. Ahmadi, Aerosol particle transport and deposition in vertical and horizontal turbulent duct flows, J. Fluid Mech. 406 (2000) 55-80.

[7] C. Marchioli, A. Giusti, M. Vittoria Salvetti, A. Soldati, Direct numerical simulation of particle wall transfer and deposition in upward turbulent pipe flow, Int. J. Multiphase Flow 29 (2003) 1017-1038.

[8] D.W.I. Rouson, J.K. Eaton, On the preferential concentration of solid particles in turbulent channel flow, J. Fluid Mech. 428 (2001) 149-169.

[9] C. Narayanan, D. Lakehal, L. Botto, A. Soldati, Mechanisms of particle deposition in a fully developed turbulent open channel flow, Phys. Fluids 15 (2003) 763.

[10] Y. Ninto, M. Garcia, Experiments on particle—Turbulence interactions in the near–wall region of an open channel flow: Implications for sediment transport, J. Fluid Mech. 326 (1996) 285-319.

[11] F. Picano, G. Sardina, C.M. Casciola, Spatial development of particle-laden turbulent pipe flow, Phys. Fluids 21 (2009) 093305.

[12] A. Soldati, C. Marchioli, Physics and modelling of turbulent particle deposition and entrainment: Review of a systematic study, Int. J. Multiphase Flow 35 (2009) 827-839.

[13] S. Balachandar, J.K. Eaton, Turbulent dispersed multiphase flow, Annu. Rev. Fluid Mech. 42 (2010) 111-133.

[14] J.D. Kulick, J.R. Fessler, J.K. Eaton, Particle response and turbulence modification in fully developed channel flow, J. Fluid Mech. 277 (1994) 109-134.

[15] M. Righetti, G.P. Romano, Particle-fluid interactions in a plane near-wall turbulent flow, J. Fluid Mech. 505 (2004) 93-121.

[16] Q. Wang, K.D. Squires, Large eddy simulation of particle-laden turbulent channel flow, Phys. Fluids 8 (1996) 1207.

[17] F. Picano, W.-P. Breugem, L. Brandt, Turbulent channel flow of dense suspensions of neutrally buoyant spheres, J. Fluid Mech. 764 (2015) 463-487.

[18] A. Tanière, B. Oesterlé, J.C. Monnier, On the behaviour of solid particles in a horizontal boundary layer with turbulence and saltation effects, Exp. Fluids 23 (1997) 463-471.

[19] G. Sardina, P. Schlatter, F. Picano, C.M. Casciola, L. Brandt, D.S. Henningson, Self-similar transport of inertial particles in a turbulent boundary layer, J. Fluid Mech. 706 (2012) 584-596.

[20] J.B. Perot, An analysis of the fractional step method, J. Comput. Phys. 108 (1993) 51-58.

[21] R.K. Shukla, M. Tatineni, X. Zhong, Very high-order compact finite difference schemes on non-uniform grids for incompressible Navier–Stokes equations, J. Comput. Phys. 224 (2007) 1064-1094.

[22] O. Desjardins, G. Blanquart, G. Balarac, H. Pitsch, High order conservative finite difference scheme for variable density low Mach number turbulent flows, J. Comput. Phys. 227 (2008) 7125-7159.

[23] X. Wu, P. Moin, Direct numerical simulation of turbulence in a nominally zero-pressure-gradient flat-plate boundary layer, J. Fluid Mech. 630 (2009) 5-41.

[24] M.P. Simens, J. Jiménez, S. Hoyas, Y. Mizuno, A high-resolution code for turbulent boundary layers, J. Comput. Phys. 228 (2009) 4218-4231.

[25] J. Lee, S.Y. Jung, H.J. Sung, T.A. Zaki, Effect of wall heating on turbulent boundary layers with temperature-dependent viscosity, J. Fluid Mech. 726 (2013) 196-225.

[26] Q. Li, P. Schlatter, L. Brandt, D.S. Henningson, DNS of a spatially developing turbulent boundary layer with passive scalar transport, Int. J. Heat Fluid Flow 30 (2009) 916-929.

[27] P. Schlatter, R. Örlü, Q. Li, G. Brethouwer, J. Fransson, A. Johansson, P. Alfredsson, D. Henningson, Turbulent boundary layers up to Reθ= 2500 studied through simulation and experiment, Phys. Fluids 21 (2009) 051702.

[28] G. Araya, L. Castillo, DNS of turbulent thermal boundary layers up to Reθ=2300, Int. J. Heat Mass Transfer 55 (2012) 4003-4019.

[29] S. Elghobashi, G.C. Truesdell, Direct simulation of particle dispersion in a decaying isotropic turbulence, J. Fluid Mech. 242 (1992) 655-700.

[30] M. Boivin, O. Simonin, K.D. Squires, Direct numerical simulation of turbulence modulation by particles in isotropic turbulence, J. Fluid Mech. 375 (1998) 235-263.

[31] L. Schiller, A. Naumann, Fundamental calculations in gravitational processing, Z. Ver. Dtsch. Ing. 77 (1933) 318-320.

[32] R. Mei, An approximate expression for the shear lift force on a spherical particle at finite Reynolds number, Int. J. Multiphase Flow 18 (1992) 145-147.

[33] C. Crowe, M. Sommerfeld, Y. Tsuji, Fundamentals of Gas-particle and Gas-droplet Flows, CRC Press, Boca Raton1998.

[34] S.I. Rubinow, J.B. Keller, The transverse force on a spinning sphere moving in a viscous fluid, J. Fluid Mech. 11 (1961) 447-459.

[35] B. Oesterle, T.B. Dinh, Experiments on the lift of a spinning sphere in a range of intermediate Reynolds numbers, Exp. Fluids 25 (1998) 16-22.

[36] S.C.R. Dennis, S.N. Singh, D.B. Ingham, The steady flow due to a rotating

sphere at low and moderate Reynolds numbers, J. Fluid Mech. 101 (1980) 257-279.

[37] O. Sawatzki, Flow field around a rotating sphere., Acta Mech. 9 (1970) 159-214.

[38] Y. Yamamoto, M. Potthoff, T. Tanaka, T. Kajishima, Y. Tsuji, Large-eddy simulation of turbulent gas-particle flow in a vertical channel: effect of considering inter-particle collisions, J. Fluid Mech. 442 (2001) 303-334.

[39] L.M. Portela, R.V.A. Oliemans, Eulerian-Lagrangian DNS/LES of particle-turbulence interactions in wall-bounded flows, Int. J. Numer. Methods Fluids 43 (2003) 1045-1065.

[40] R.J. Adrian, C.D. Meinhart, C.D. Tomkins, Vortex organization in the outer region of the turbulent boundary layer, J. Fluid Mech. 422 (2000) 1-54.

[41] C. Ching, L. Djenidi, R. Antonia, Low-Reynolds-number effects in a turbulent boundary layer, Exp. Fluids 19 (1995) 61-68.

[42] C. Rogers, J. Eaton, The behavior of solid particles in a vertical turbulent boundary layer in air, Int. J. Multiphase Flow 16 (1990) 819-834.

[43] R.G. Jacobs, P.A. Durbin, Simulations of bypass transition, J. Fluid Mech. 428 (2001) 185-212.

[44] T. Sayadi, C.W. Hamman, P. Moin, Direct numerical simulation of complete H-type and K-type transitions with implications for the dynamics of turbulent boundary layers, J. Fluid Mech. 724 (2013) 480-509.

[45] J.C.R. Hunt, A.A. Wray, P. Moin, Eddies, streams, and convergence zones in turbulent flows, Proceedings of Summer Program, Standford University, 1988, pp. 9-14.

[46] C. Smith, A Synthesized Model of the Near-wall Behavior in Turbulent Boundary Layers, DTIC Document, 1984.

[47] T. Theodorsen, Mechanism of turbulence, Proceedings of the Second Midwestern Conference on Fluid Mechanics, Ohio State University, 1952, pp. 1-18.

Table 1

Parameters of the tracked particles for the particle-laden cases studied.

Case	St	Φ_m	d_p^+	$N_{p,total}$	$\Delta y_{min}/d_p$	η_{min}/d_p
A	10	0.1	0.1472	6.28×10^8	4.7	9.0
B	10	1.0	0.1472	6.28×10^9	4.7	9.0
C	50	1.0	0.329	5.6×10^8	2.1	4.0

Figure Captions

Fig. 1. Schematic of particle-laden turbulent boundary layer flow over a flat plate.

Fig. 2. (a) Mean streamwise velocity profile. (b) Turbulence intensities profiles. Lines are from the present DNS at $Re_\theta = 900$. Solid line, mean streamwise fluid velocity $\overline{u}^+$ in (a) and streamwise turbulence intensity u'^+_{rms} in (b); dashed line, wall-normal turbulence intensity v'^+_{rms}; dash-dot line, spanwise turbulence intensity w'^+_{rms}; solid circle, Ching et al. [41] at $Re_\theta = 979$; open circle, Ching et al. [41] at $Re_\theta = 765$; triangle, Adrian et al. [40] at $Re_\theta = 930$; diamond, Wu and Moin [23] at $Re_\theta = 900$.

Fig. 3. (a) Mean streamwise particle velocity and (b) particle streamwise fluctuating velocity versus the outer coordinate y/δ^*, where δ^* is the local displacement thickness.

Fig. 4. Mean streamwise particle velocity profiles in the turbulent region at $x = 4867\theta_0$. (a) In inner wall coordinate y^+. (b) In outer coordinate y/δ.

Fig. 5. Relative mean streamwise velocity between particles and fluid in inner wall units at $x = 4867\theta_0$, using a semi-logarithmic scale.

Fig. 6. Particle fluctuating velocities and Reynolds stress versus the inner wall coordinate y^+ in the turbulent region at $x = 4867\theta_0$: (a) streamwise component $u'^+_{p\,rms}$; (b) wall-normal component $v'^+_{p\,rms}$; (c) spanwise component $w'^+_{p\,rms}$; (d) Reynolds stress $-\overline{u'_p v'_p}^+$. The velocity fluctuations and Reynolds stress of the fluid phase are also reported for comparison.

Fig. 7. Instantaneous distributions of the particle populations with $St = 50$, superposed on the local streamwise vorticity field ω_x. The vectors represent the particle velocity in the y-z plane at $x = 4867\theta_0$ and the colored contours map the values of the instantaneous streamwise vorticity. Note that particles are drawn as solid circles, larger than the real scales for better visualization. Red particles migrate towards the wall whereas white particles move away from the wall.

Fig. 8. Wall-normal profile of the ratio between the particle turbulent kinetic energy K_p and the fluid turbulent kinetic energy K_f at $x = 4867\theta_0$.

Fig. 9. Variation of the particle concentration very close to the wall C_w along the plate versus (a) the streamwise coordinate x/θ_0 and (b) the momentum thickness Reynolds number Re_θ.The skin-friction coefficient C_f is also included in this figure for comparison. Note that C_f is multiplied by 10^4.

Fig. 10. Instantaneous isosurfaces of the second invariant of the velocity gradient tensor, Q, colored by the local streamwise fluid velocity ($Q = 10^{-4}$). These sub-images are taken at the same time from case B and each represents a typical streamwise zone. (a) In the laminar region $600\theta_0 \le x \le 1200\theta_0$. (b) In the transitional region $1400\theta_0 \le x \le 2200\theta_0$. (c) In the early turbulent region $2200\theta_0 \le x \le 3000\theta_0$. (d) In the fully developed turbulent region $5000\theta_0 \le x \le 5800\theta_0$.

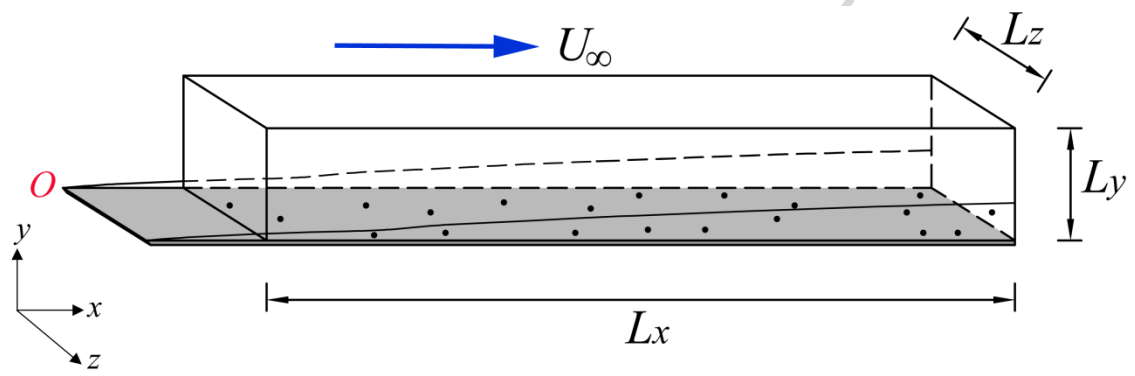

Fig. 1

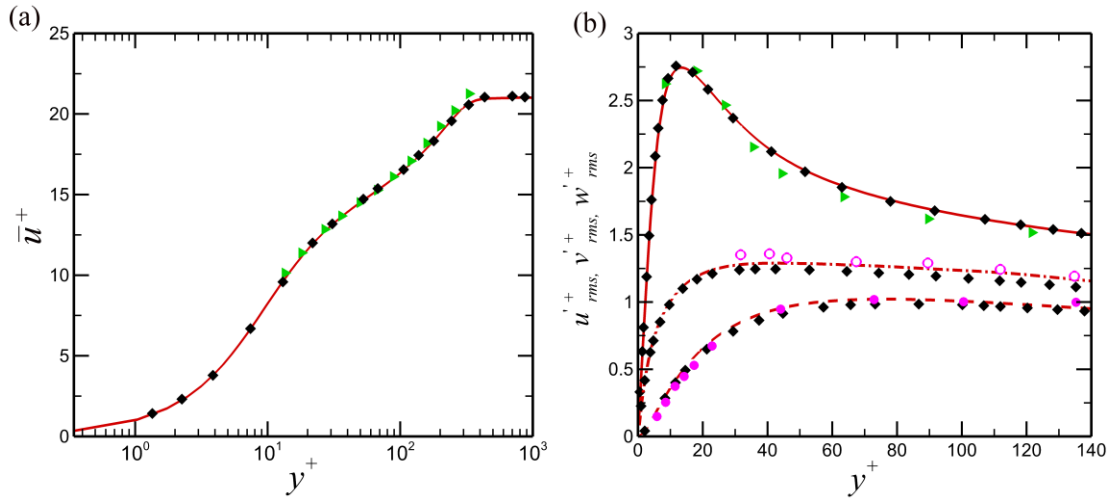

Fig. 2

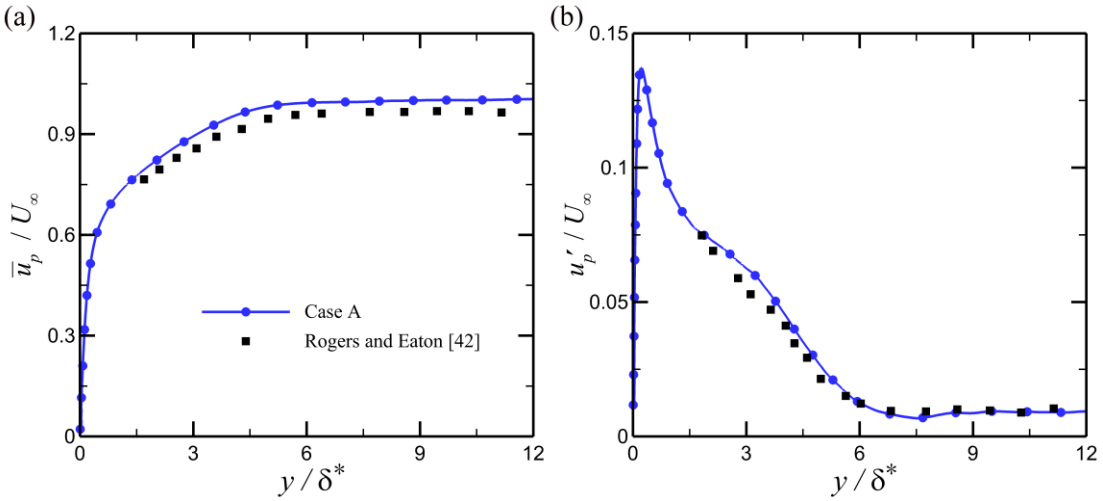

Fig. 3

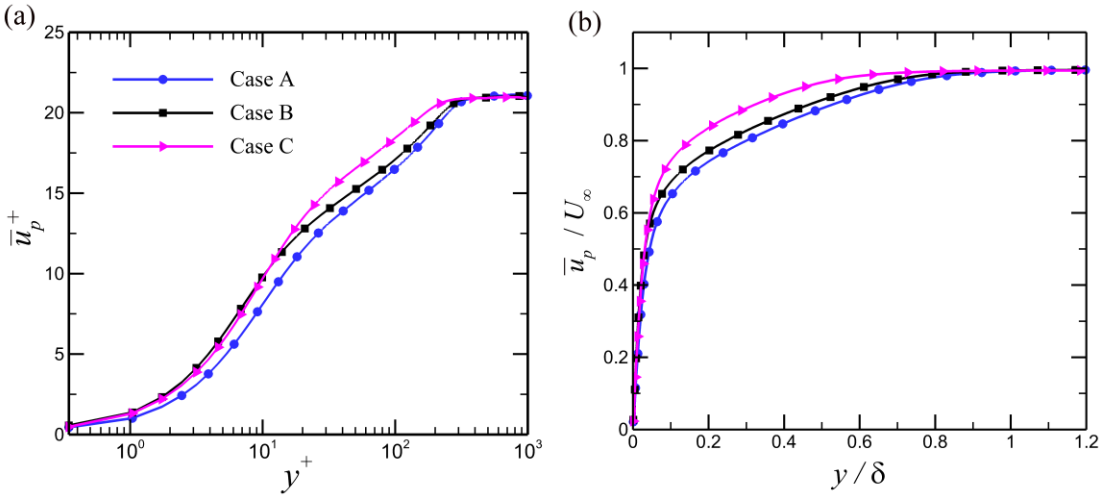

Fig. 4

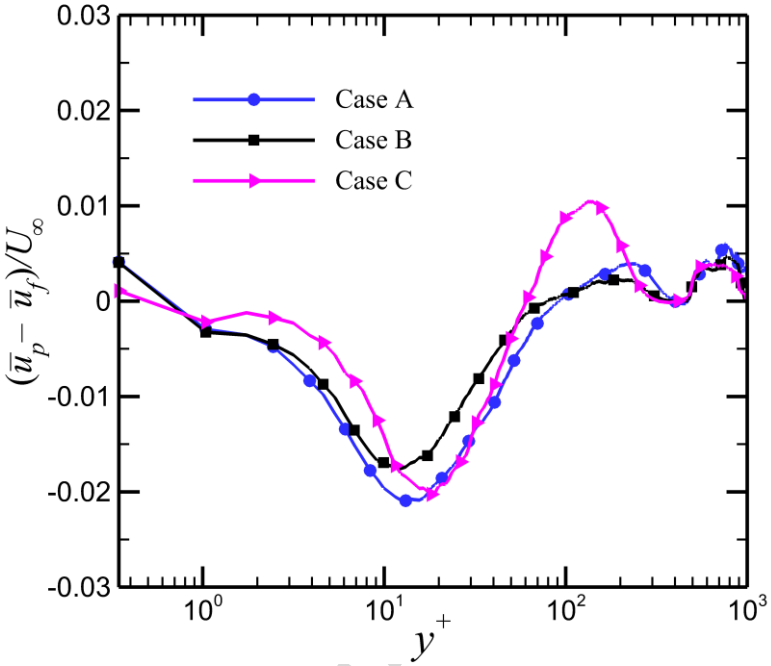

Fig. 5

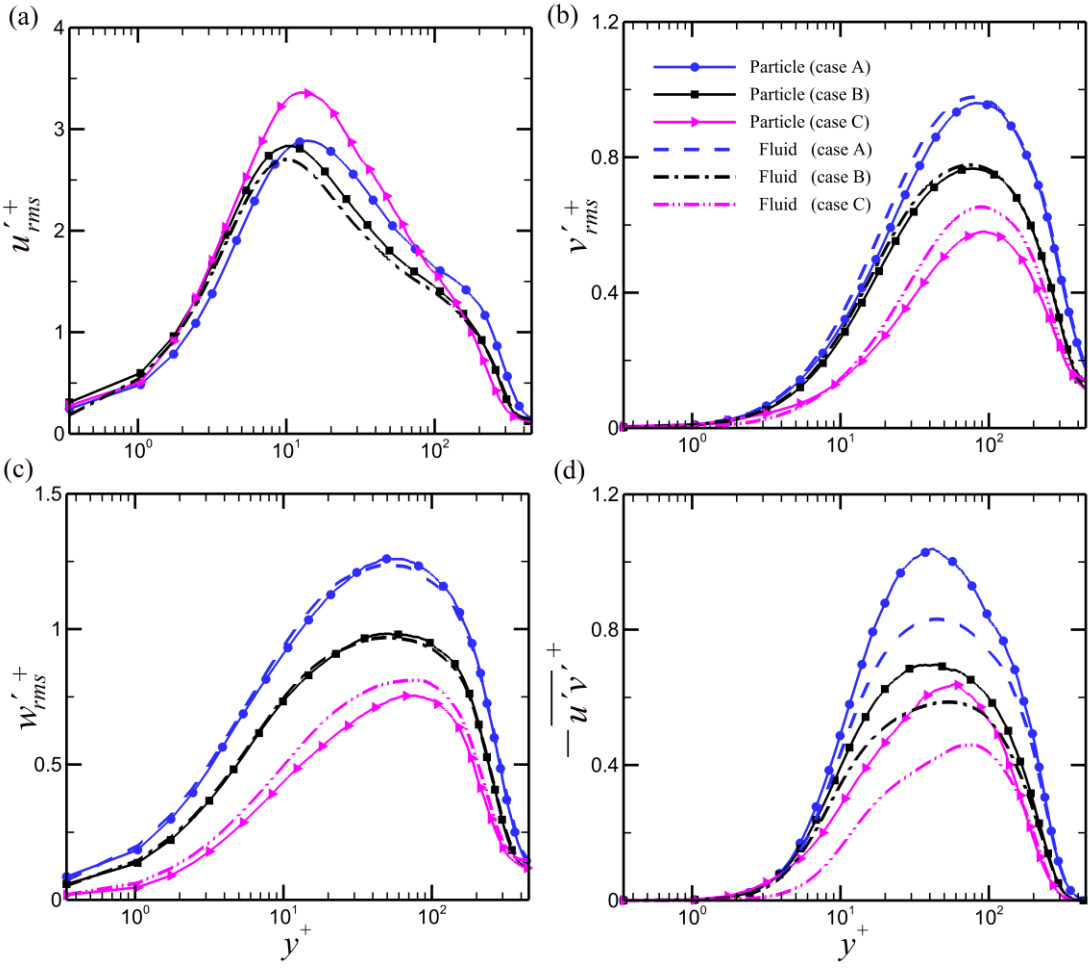

Fig. 6

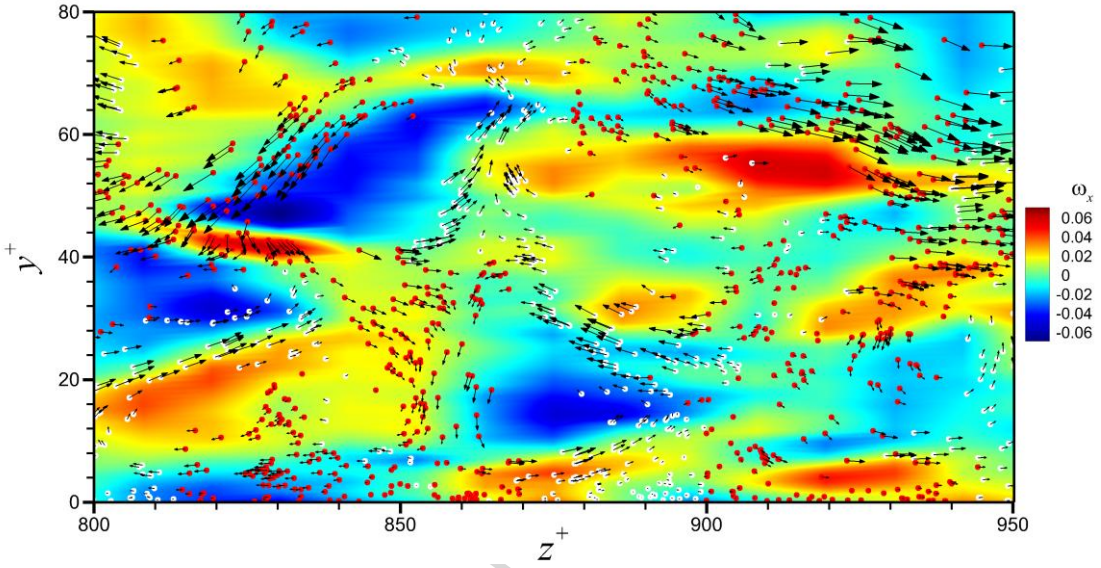

Fig. 7

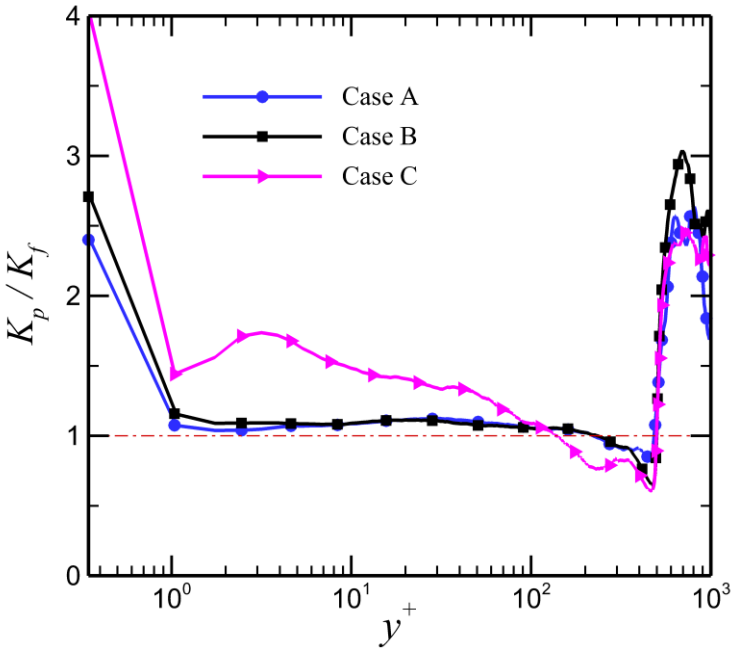

Fig. 8

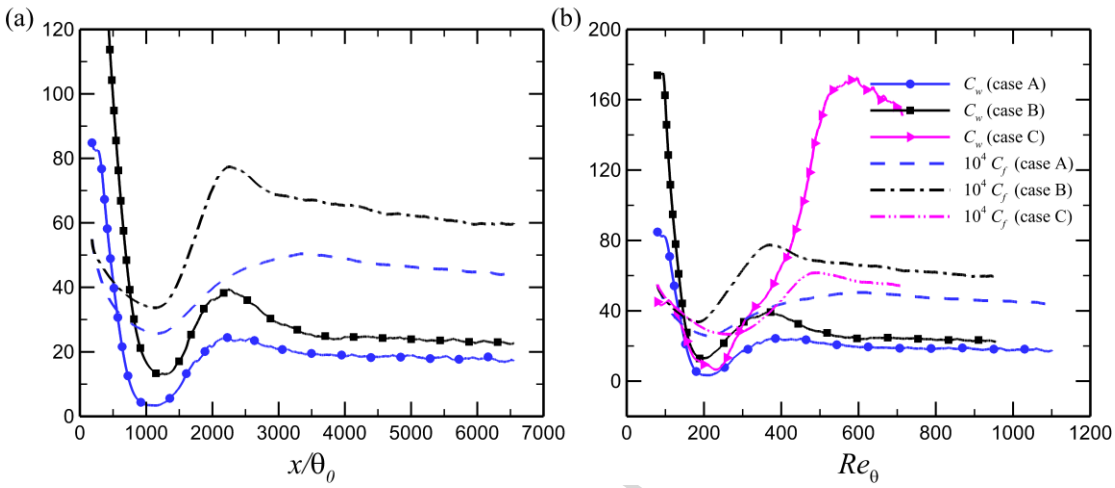

Fig. 9

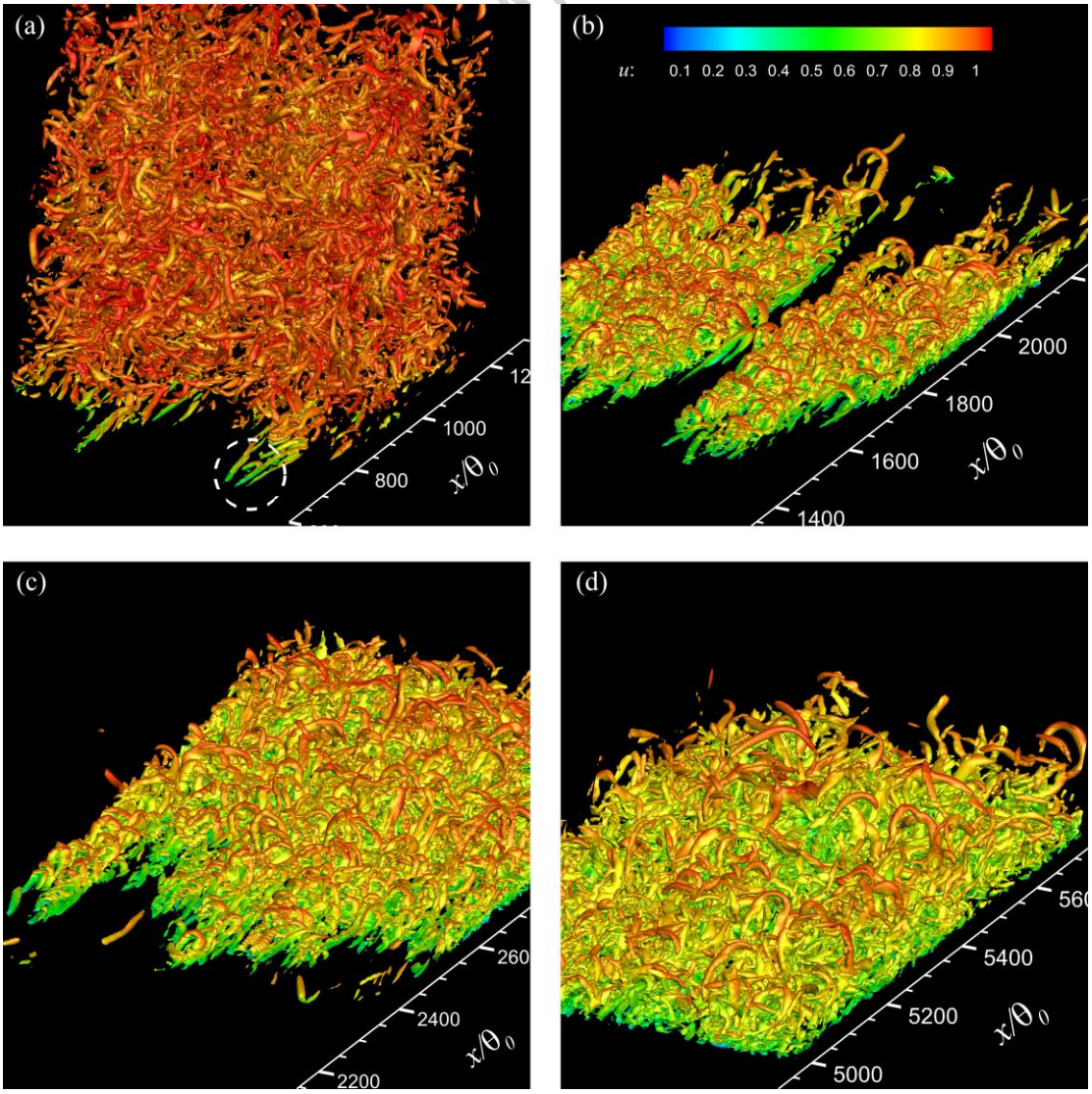

Fig. 10

Graphical abstract

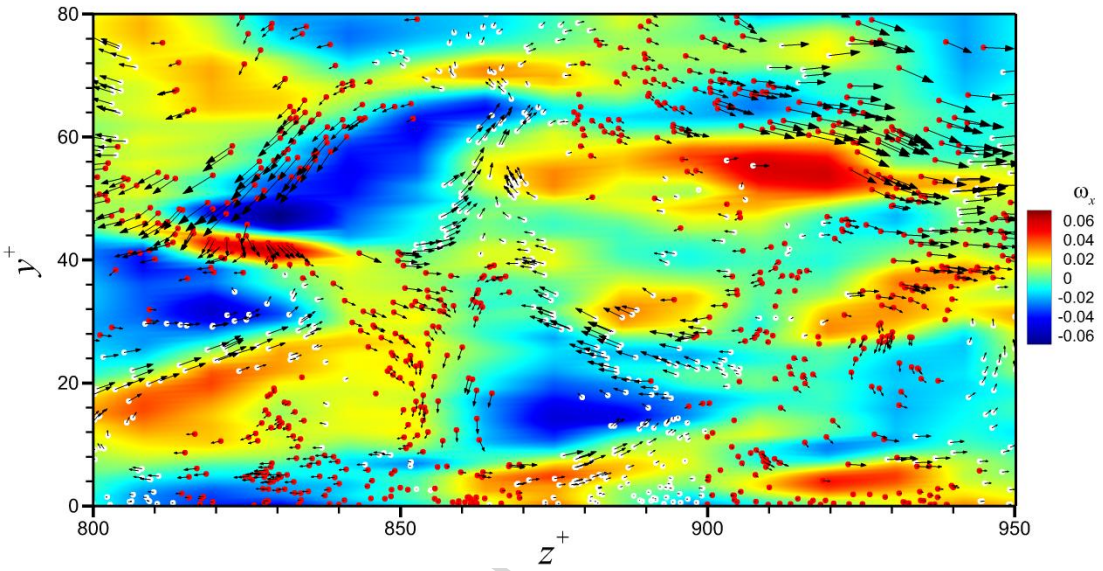

Highlights

Particle statistics in a spatially developing boundary layer are investigated.

Particle behavior is associated with inertia and near-wall vortical structures.

The spatial evolution of wall concentration is similar to that of the skin-friction.

Particle wall concentration decreases slowly as the flow develops downstream.